AIAA 95-0737

Experimental Results on the Feasibility of an Aerospike for Hypersonic Missiles

Lawrence D. Huebner
NASA Langley Research Center
Hampton, VA

Anthony M. Mitchell and Ellis J. Boudreaux
USAF Wright Laboratory
Eglin Air Force Base, FL

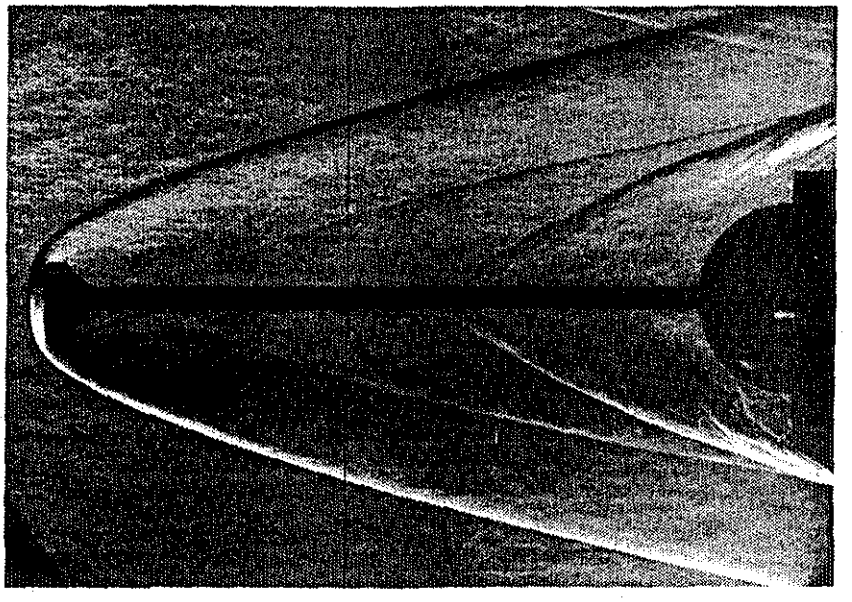

33rd Aerospace Sciences Meeting and Exhibit
January 9-12, 1995 / Reno, NV

EXPERIMENTAL RESULTS ON THE FEASIBILITY OF AN AEROSPIKE FOR HYPERSONIC MISSILES

Lawrence D. Huebner*
NASA Langley Research Center

Anthony M. Mitchell† and Ellis J. Boudreaux**
Wright Laboratory/Eglin Air Force Base

Abstract

A series of wind tunnel tests have been performed on an aerospike-protected missile dome at a Mach number of 6 to obtain quantitative surface pressure and temperature-rise data, as well as qualitative flow visualization data. These data were used to determine aerospike concept feasibility and will also provide a database to be used for calibration of computational fluid dynamics codes. Data were obtained on the hemispherical missile dome with and without an aerospike that protrudes ahead of the dome along the axisymmetric center line. Data were obtained on two models (one pressure, one temperature) in the NASA Langley 20-Inch Mach 6 Tunnel at a freestream Reynolds number of 8.0×10^6/ft and angles of attack from 0 to 40 degrees. Surface pressure and temperature-rise results indicate that the aerospike is effective for very low angles of attack (<5 degrees) at Mach 6. Above 5 degrees, impingement of the aerospike bow shock and the flow separation shock from the recirculation region created by the aerospike causes pressure and temperature increases on the windward side of the dome which exceed values observed in the same region with the aerospike removed. Flow characterization obtained via oil-flow and schlieren photographs provides some insight into the quantitative surface data results, including vortical flow and shock-wave impingement.

Nomenclature

M_∞	freestream Mach number
p	static pressure (psia)
p_∞	freestream pressure (psia)
Re_∞	freestream Reynolds number
s	arc length along model surface measured radially from the dome/axisymmetric centerline intersection (in)
X_{body}	streamwise distance along body (see Fig. 4) (in)
α	angle of attack (deg)
Δt	time interval as measured from beginning of model injection (sec)
ΔT	temperature rise (see Eq. 1) (°F)
ϕ_{RAY}	data-ray angle (see Fig. 3) (deg)

Introduction

The aerospike concept is proposed as a promising dome assembly design for high-speed tactical guided missiles. The concept was first conceived in the 1950s as a means of reducing the heat transfer rates and aerodynamic drag on axisymmetric blunt bodies[1-4]. In fact, the spiked-nose concept was successfully incorporated into the design of the C-4 and D-5 trident missiles and reduced the drag of these vehicles by up to 50% at Mach numbers as high as 8[5]. At Mach numbers from 3 to 8, the surface pressures and aerothermodynamic heating rates collectively may be severe enough to cause failure of the hemispherical dome material. Conceptually, the aerospike creates a conical region of recirculatory flow in front of the hemisphere dome that shields and protects it from the oncoming freestream flow. Furthermore, an addition to the end of the aerospike, known as an aerodisk, can be used to allow a fixed length aerospike to be effective over a wide range of Mach numbers by fixing the separation of the boundary layer near the front of the aerospike which creates the recirculation region regardless of Mach number. The aerospike/aerodisk configuration, along with the induced flowfield, is shown schematically in figure 1. The configuration consists of a hemispherical dome mounted to a cylindrical body. Attached to the dome along the axisymmetric centerline is the aerospike/aerodisk assembly. At low hypersonic

* Aerospace Engineer, Hypersonic Airbreathing Propulsion Branch, Gas Dynamics Division, MS 168, Hampton, VA 23681-0001, AIAA Senior Member.

† Research Engineer, USAF Wright Laboratory, Armament Directorate, Eglin AFB, FL 32542-5434, AIAA Member.

** Senior Research Engineer, USAF Wright Laboratory, Armament Directorate, Eglin AFB, FL 32542-5434.

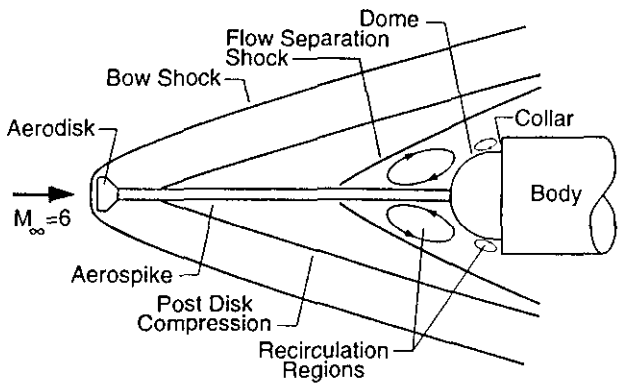

Fig. 1. Schematic of aerospike-induced flowfield.

speeds and $\alpha = 0°$, a detached bow shock stands out in front of the aerodisk and remains away from the dome. As the flow behind the bow shock expands around the aerodisk, a weak compression is formed at its base. The wake flow caused by the aerodisk and the nearly stagnant flow near the dome creates the conically-shaped recirculation region shown. The region is separated from the inviscid flow within the bow shock by a flow separation shock. This shock isolates the recirculation region which effectively reduces the pressure and heating distributions on the hemispherical dome and also allows them to be more uniform[6]. Furthermore, this configuration has a body with a larger diameter than the dome, creating the potential for additional flow recirculation in the region near the front face of the body (referred to as the collar) and the side of the dome.

For non-zero angles of attack, the flowfield is further altered by a lee-side vortex structure that is influenced by the presence of the aerospike. The separated, vortical flow region in front of the dome is unsteady, which may cause structural fatigue at the aerospike attachment region[4]. Furthermore, the variation in model wall temperature during a tunnel run will affect the state of the aerospike boundary layer and subsequent separation shock at the foremost edge of the recirculation region. All of these phenomena may influence the dome surface aerothermal characteristics.

The objectives of the current study are twofold. First, concept feasibility will be addressed by measuring and analyzing surface pressures and temperatures on the dome and on the forward part of the cylindrical body. These data, along with qualitative flow characterization data (oil-flow and schlieren photographs), will confirm or deny the aforementioned benefits of the concept and allow for better understanding of aerospike flowfield physics. The second objective of the study will be to create a database applicable for calibrating computational fluid dynamic codes that will be used to predict these types of hypersonic flows. This paper will concentrate on the presentation and discussion of the data obtained in the NASA Langley 20-Inch Mach 6 Tunnel. A description of the test facility, test article, instrumentation, and qualitative data obtained will be presented, followed by a discussion of the results.

Test Facility

The tests were performed in the NASA Langley Research Center 20-Inch Mach 6 Tunnel. This wind tunnel is a hypersonic blowdown facility that exhausts the air test medium either to the atmosphere (with the aid of an annular air ejector) or to vacuum spheres. The operating conditions for the tunnel are stagnation pressures of 30 to 525 psia, stagnation temperatures of 810° to 1018°R, and freestream Reynolds numbers of 0.5 to 9.0 x 10^6/ft. The wind tunnel has a two dimensional, fixed-geometry, contoured nozzle that is 7.45 ft long to provide the nearly constant nominal Mach 6 flow. The test section is 20.5 by 20 inches and is fitted with two quartz windows for schlieren observation that are 17 inches in diameter. Typical run times are 5-10 minutes when the air exhausts to the vacuum spheres, depending on freestream Reynolds number. To avoid tunnel startup/shutdown transients, the model is injected into the test section, after proper wind tunnel test conditions are achieved. The model is injected by a manually-operated, remotely-controlled injection system. Injection time of the model is approximately one second. A detailed description of this tunnel is presented in reference 7.

For this study, the test conditions were a stagnation pressure of 475 psia and a stagnation temperature of 875°R, yielding a freestream Mach number of 6.06 and a freestream Reynolds number of 8.0x10^6/ft.

Test Article

The aerospike model surface geometry is shown in figure 2. The material used for the model was 17-4 PH, H900 stainless steel. It consists of a 4-inch long, 4-inch diameter cylindrical body and a 3-inch diameter hemispherical dome. The dome is offset from the body with a 0.25-inch long, 3-inch diameter cylindrical extension. The model design allows for the testing of the model with or without an aerospike, which is threaded at the base and screws into the dome. The aerospike as used in this series of tests consisted of a 12-inch long aerospike/aerodisk assembly, hereafter referred to as simply 'the aerospike.'

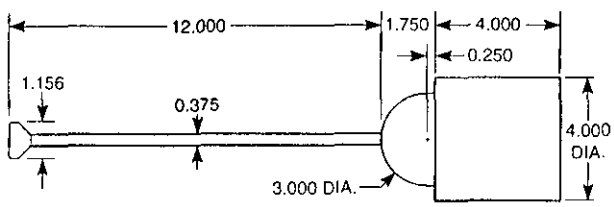

Fig. 2. Aerospike surface geometry dimensions (in inches).

Instrumentation

The critical data from these tests were the surface pressure and temperature measurements over a range of pitch and roll angles. Two separate models were fabricated to obtain these data; the pressure model contained 51 0.041 ID pressure orifices, and the temperature model contained 30 3-lead coaxial thermocouples. (A third uninstrumented model was also used for surface oil-flow visualization.) The orifices and thermocouples were placed along three rays that (at 0-degree roll) corresponded to the upper and lower vertical centerline rays and the ray halfway between them on the model left side (see Fig. 3). Fig. 3 also shows that, by setting the model

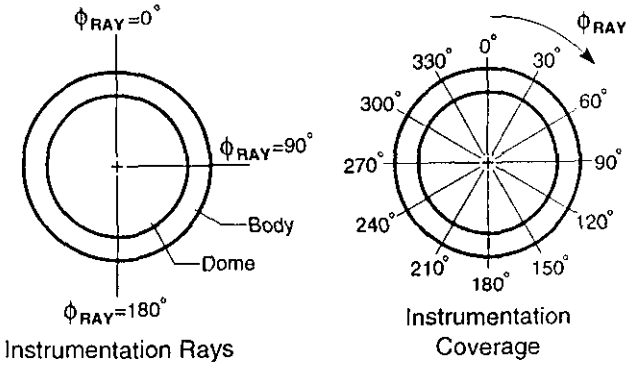

Fig. 3. Aerospike instrumentation orientation, looking aft.

at one of six specific roll angles, data acquisition coverage was obtained along rays every 30° over the entire dome. The pressure model had 17 orifices (8 on the dome and 9 on the body) along each ray, while the temperature model had 10 thermocouples (9 on the dome and one on the body) along each ray. Nominal locations of this instrumentation are presented in Fig. 4, with the pressure instrumentation layout shown only on the upper half and the thermocouple layout shown only on the lower half of the figure for clarity.

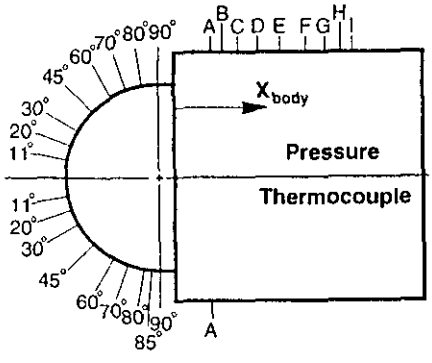

Gauge	X_{body}
A	0.594
B	0.781
C	1.031
D	1.344
E	1.719
F	2.124
G	2.436
H	2.686
I	2.873

Fig. 4. Aerospike instrumentation locations (linear dimensions in inches).

The pressure orifices made up the terminal end of approximately two feet of stainless steel tubing that were connected to about six feet of temperature resistant plastic tubing. These were directly connected to one of two 15-psid electronically-scanned pressure (ESP) transducer modules. For each data point, the pressure was acquired 10 times per second for two seconds, and an average steady-state pressure was calculated. Prior to each run the two ESP modules were calibrated, and a number of preset wind-off, pumpdown points were recorded to compare the pressures measured by the ESP modules to the tunnel wall static pressure, as measured by a 15-psia Druck transducer. Differences were noted and used in the final reduction of the pressure data. Pressure settling times were determined by running the aerospike configuration and taking data every five seconds for twenty seconds. The flow was assumed settled when the pressures varied by less than 0.03 psia, which is the specified accuracy of the 15-psid ESP modules. Using this criterion, the settling time was determined to be 10 seconds. Therefore, pressure data were recorded 10 seconds after the model was injected or subjected to an angle-of-attack change.

The thermocouples used in this investigation were 0.063-inch diameter Medtherm chromel/constantan coaxial surface thermocouples with a second in-depth constantan wire to provide a backwall temperature reading 0.25 inches below the surface. (The purpose of the backwall temperatures were to provide boundary condition data for heat-transfer calculations.) A schematic of the thermocouple assembly is shown in figure 5. In

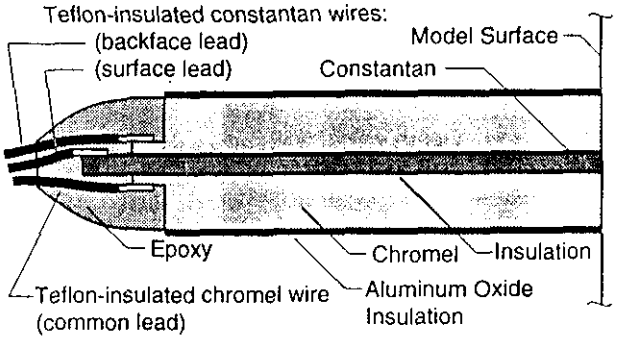

Fig. 5. Schematic of three-lead thermocouple assembly.

order to insure the accuracy of the electric signal from the thermocouple, each coaxial gauge was insulated from the stainless steel model with a 4-5 mil thick coating of aluminum oxide. Measurements were taken prior to testing to confirm the electrical resistance of each thermocouple to greater than 20MΩ. Continuous data were obtained during temperature measurements. The data acquisition was initiated just prior to model injection into the Mach 6 flow and ended following model retraction, resulting in between 20-25 seconds of data were taken at a frame rate of 50 frames per second. Although this is more data than required for determining surface heat-transfer values, there was interest in the maximum temperature achieved in this amount of time.

One goal of this study was to use the temperature data obtained to determine heat transfer for each gauge. However, the data-reduction program first chosen for this purpose was not robust enough to calculate the two-dimensional or three-dimensional conductive heat transfer, as well as radiative effects. Instead, surface temperature-rise data will be presented, showing a datum for each surface thermocouple for a given run. Even though heat-transfer values have not been calculated, temperature-rise data are still relevant for aerospike concept feasibility assessment for hypersonic missiles because the temperature-rise data provide a straightforward understanding of the local aeroheating that develops. The temperature-rise data for each thermocouple were computed as:

$$\Delta T = T_{\Delta t = 3\ sec} - T_{\Delta t = 0\ sec}, \qquad (1)$$

where Δt is the change in time from the beginning of model injection. Since model injection time was less than one second, the thermocouple data to be presented were exposed to the Mach 6 freestream flow for over two seconds to allow for the aerothermodynamic influence without significant model heat soaking.

Qualitative Data Obtained

Two qualitative types of data were also obtained on the aerospike configuration. First, schlieren photographs and videos were taken of the flow over the model with the aerospike both on and off. These provided visualization of the flowfield density gradients generated with and without the spike. The video allowed study of the unsteady phenomena in the flowfield. Second, surface oil-flow photographs were taken post-run using the geometrically-identical, uninstrumented aerospike model with the aerospike both on and off. These oil-flow data were obtained using a pigmented oil-droplet technique. In this procedure, a light coat of flat black paint is sprayed on the model, which is then coated with a layer of clear oil. Next, small droplets of white-pigmented oil are speckled onto the model. The model is injected into the test section for a period of three to seven seconds to allow the flow patterns to develop. The post-run patterns are then photographed. These qualitative data will be used where appropriate to supplement pressure and temperature results as well as the help in the assessment of the nature of the fluid physics in the flowfield.

Results

Pressure, temperature-rise, and flowfield data from the dome will be presented at specific angles of attack, comparing spike-on data with spike-off data to facilitate the objective of determining aerospike concept feasibility. The angles of attack chosen for discussion in this paper are 0°, 5°, 10°, 20°, and 40°. Data were also recorded at 7.5°, 12°, 15°, 25°, 30°, and 35°. Symmetry checks at ray locations mirroring the vertical centerplane were made for the spike-on and spike-off configurations with these data, which indicated that there is good symmetry and data repeatability for these configurations at all angles of attack. Therefore, data will be presented only for ϕ_{RAY} angles from 0° to 180°. Schlieren and oil-flow photographs will also be presented to augment the surface data results. Furthermore, analysis of the data indicated that there was no significant difference seen in pressure or temperature-rise data on the body with or without the aerospike. So, only data on the hemispherical dome surface will be presented in this paper.

Feasibility Assessment at $\alpha = 0°$

Figure 6 compares spike-on vs. spike-off data at α=0°. Parts 'a' and 'b' of this and subsequent figures have seven plots to show the rays of data every 30 degrees from ϕ_{RAY}=0° to 180°. Part 'a' presents surface pressure data, while part 'b' presents temperature-rise data. The pressure data are normalized by freestream pressure to reduce any pressure variations caused by small changes in the tunnel conditions during the run. These data are plotted versus arc length, s, which is zero at the foremost part of the dome and is measured along the surface of the dome. For reference, the dome/body intersection corner is located at s=2.61 inches. The squares denote the spike-on data and the circles denote the spike-off data.

At α=0°, a significant reduction in dome pressures and a lower temperature rise are seen for all rays with the aerospike on, confirming the advantages of the aerospike at this condition. Note also the good axisymmetry of the data at α=0° by comparing data from each ray with the others.

The schlieren photograph of the spike-off model shows the detached Mach 6 bow shock standing in front of the dome. A small separation region near the dome shows the foremost extent of boundary-layer separation due to the collar of the body. In this region, the pressures stabilize and the temperature rise increases only slightly along the rest of the dome. With the spike on, the bow shock from the aerospike is far from the dome, and the dome is completely enveloped within the large recirculation region. The schlieren video at this condition showed that the boundary of this region is slightly unsteady. Comparisons of oil-flow photographs of the dome for the two configurations shows the spike-off stagnation region at the tip of the dome and the accumulation of oil denoting the forward extent of the dome/collar separation region, as well as the spike-on low shear area near the base of the aerospike and the movement of the surface flow toward the base of the aerospike. A

concentric vortical flow pattern is seen near the dome/collar interface with the spike on, causing the slight increase in temperature rise there due to the boundary-layer separation. (The two spots on these and all other oil-flow photographs are lighting reflections recorded on the film and are not part of the oil-flow patterns.)

These data confirm that the aerospike is truly providing an advantage in terms of pressure and thermal loading reductions on the dome at $\alpha=0°$.

Feasibility Assessment at $\alpha = 5°$

At $\alpha=5°$ (Fig. 7), the aerospike still maintains beneficial pressure and temperature-rise distributions on the leeward side of the configuration and near the dome tip on the windward side. However, the spike-on pressures increase to and eventually slightly exceed the spike-off pressures away from the dome tip for $\phi_{RAY}=120°$ to 180°. Furthermore, spike-on temperature-rise values are at some places over twice that observed with no spike.

The cause for the loss in aerospike effectiveness can be seen by studying the qualitative data. The schlieren and oil-flow photographs show a flowfield structure similar to the $\alpha=0°$ case for the spike off, while evidence of separation-shock impingement on the dome is seen for the spike-on model. This results in a complex, unsteady, local flowfield near the lower centerline. Note also, in the spike-on oil-flow photograph, that a large low-shear region exists on the leeward side of the dome and results in the low pressure and temperature-rise values there.

Thus, the beneficial effects provided by the aerospike are constrained to much lower angles of attack than expected due to the detrimental effects of separation-shock impingement on the windward surface observed at $\alpha=5°$. It was expected that these beneficial results would exist until bow-shock impingement on the dome occurred.

Feasibility Assessment at $\alpha = 10°$

At $\alpha=10°$ (Fig. 8), the beneficial pressures and temperature rises are limited to $\phi_{RAY}\leq 60°$. In fact, on the rest of the dome, the spike-on configuration pressures and temperature rises actually exceed those of the spike-off configuration, aside from the region very near the dome/aerospike intersection. Note that some data exceed the maximum range on the plots. For some of the orifices at certain angles of attack, the pressure reading exceeded the maximum pressure of 15-psi that were able to be measured by the ESP modules. Although the magnitude of pressure increase for the spike-on configuration is not significantly greater than that for spike-off, temperature-rise values for spike-on are over 4 times higher than spike-off values just below the base of the aerospike, at $\phi_{RAY}=180°$.

The leeward effects of the aerospike include an unsteady separation shock, a low-shear region that occupies less of the dome and more of the forward-facing collar of the body than at $\alpha=5°$, as well as evidence of vortex formation beginning on the dome. The spike-on schlieren photograph shows the separation shock below the aerospike that once again impinges on the dome. The location of impingement away from the vertical centerline is seen clearly on the spike-on, oil-flow photograph. This confirms that the cause of the pressure and temperature-rise increases at $\alpha=10°$ is also due to separation-shock impingement, but at stronger levels than at $\alpha=5°$.

Feasibility Assessment at $\alpha = 20°$

At $\alpha=20°$ (Fig. 9), beneficial pressure and temperature-rise data are only observed for $\phi_{RAY}\leq 30°$. At this condition, the extent of the leeward separation shock is nearly perpendicular to the body axis and is quite unstable since it is in the wake of the aerodisk. The leeward side of the spike-off configuration contains a vortical pattern on the dome and body collar, as seen in the oil-flow photograph. Propagation of this pattern into the flowfield is seen in the schlieren photograph.

On the windward side, a new flowfield pattern has developed in that the shock from the aerodisk now interacts with the post-disk compression shock and propagates along the length of the aerospike shaft. A small shock region still develops near the base of the aerospike, and the shock/shock interaction and impingement on the dome causes excessive pressure and heating loads there. In fact, the local flow conditions are so strong near the base that, after only 5 sec in the flow during oil-flow runs, they caused the oil coating the dome to dissipate completely from that region, as seen in the dull region below the aerospike attachment point on the spike-on, oil-flow photograph. Clearly, bow shock impingement on the dome is as severe aerothermodynamically as separation-shock impingement.

Feasibility Assessment at $\alpha = 40°$

At $\alpha=40°$ (Fig. 10), the region of influence of the aerospike is reduced to only small regions near the base of the aerospike and the leeward centerline. In fact, pressure and temperature-rise data for the spike-on case collapse to the spike-off data away from the dome/aerospike intersection, even on the leeward side. Confirmation of this is observed in the qualitative data. Comparing schlieren photographs, the strong shock and wake from the aerodisk propagate beyond the dome without impingement. Furthermore, the flow near the dome shows very similar features, especially on the windward side. A weak recirculation region is evident on the leeward side, but a shock from the dome is also formed. These similarities can also be seen in the oil-

flow photographs, including the stagnation regions on the windward centerline, vortical flow near the dome/body intersection, and the low-shear, vortical region on the leeward side.

Conclusions

A set of wind tunnel tests were performed to determine the feasibility of using an aerospike to reduce the pressure and thermal loading on the hemispherical dome of future hypersonic missiles. Pressure and temperature data were obtained at Mach 6 and compared for configurations with and without an aerospike. Flow visualization data were used to augment the pressure and temperature-rise data and provide an understanding of the flowfield characteristics. The data are available for use in computational fluid dynamics code calibration for these types of flows.

Results from the surface pressure and temperature-rise data at this Mach number indicate that a limit exists to the configuration attitude that provides a completely beneficial flowfield in the presence of an aerospike. From this study at Mach 6, limiting angles of attack to below 5° should provide pressure and thermal loadings that are at or below the levels seen for hemispherical domes with no spike. The limiting factor in the angle-of-attack capabilities of this concept is the impingement of the separation shock on the dome created by the aerospike. Aerospike shock impingement on the dome is particularly strong (in terms of pressure and temperature) at high angles of attack.

A secondary conclusion discovered from these data involves the influence of the collar on the dome pressures and temperatures near the body. This collar creates small flow recirculation regions that cause pressures to level off and temperature rises to increase slightly along the dome surface.

References

1. Stalder, Jackson R.; and Nielsen, Helmer V.: "Heat Transfer from a Hemisphere-Cylinder Equipped with Flow-Separation Spikes," NACA TN 3287. September 1954.

2. Bogdonoff, Seymour M.; and Vas, Irwin E.: "Preliminary Investigations of Spiked Bodies at Hypersonic Speeds," *Journal of the Aero/Space Sciences*, Volume 26, Number 2, February 1959, pp. 65-74.

3. Crawford, Davis H.: "Investigation of the Flow Over a Spiked-Nose Hemisphere-Cylinder at a Mach Number of 6.8," NASA TN D-118, December 1959.

4. Reding, J. P.; Guenther, R. A.; and Richter, B. J.: Unsteady Aerodynamic Considerations in the Design of a Drag-Reduction Spike. *Journal of Spacecraft and Rockets*, Volume 14, Number 1, January 1977, pp. 54-60.

5. Reding, J. P.; and Jeemen, D. M.: An Advanced Aerospike to Minimize Nose Drag. Lockheed Horizons, Volume 15, 1984, pp. 46-54.

6. Winderman, J. B.; Drake, P.A.; et al.: "IR/RF Dome Technology Report, General Dynamics Volume I, Concept Definition and Preliminary Design," WL/MN-TR-91-46, Volume I, November 1992.

7. Keyes, J. W.: Force Testing Manual for the Langley 20-Inch Mach 6 Tunnel. NASA TM-74026, 1977.

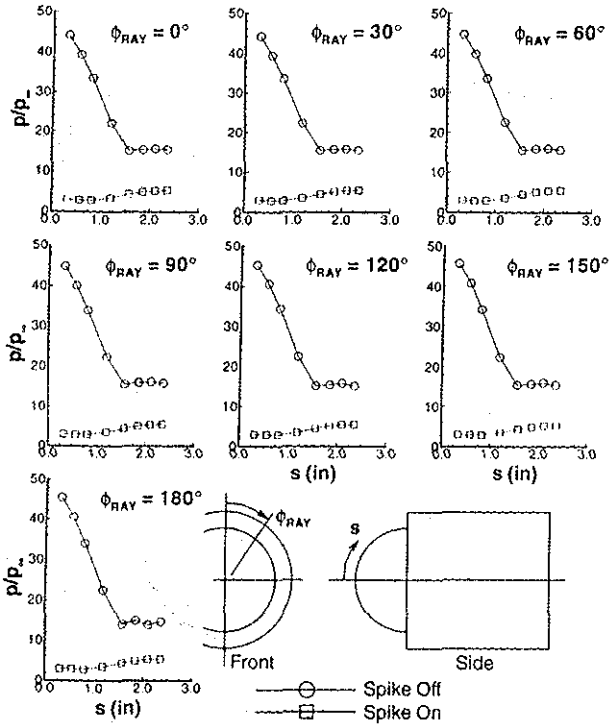

Figure 6a. Comparison of spike-off vs. spike-on surface pressure distributions, $\alpha = 0°$.

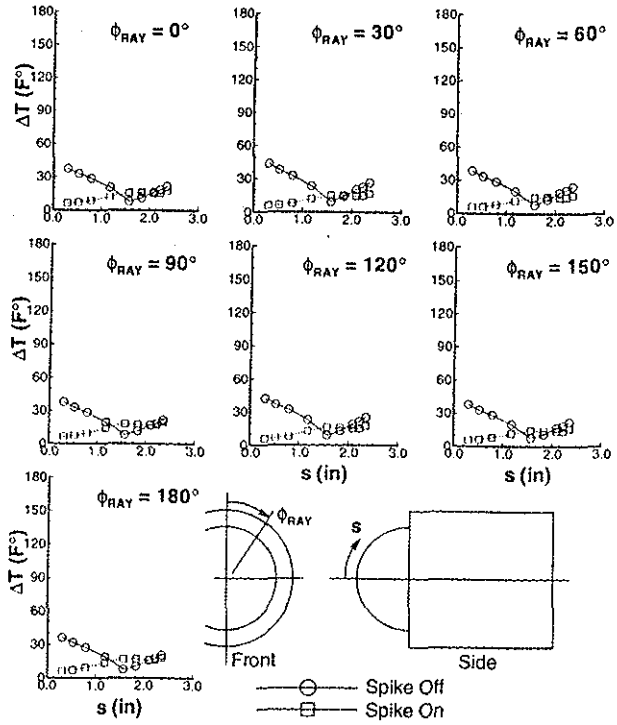

Figure 6b. Comparison of spike-off vs. spike-on surface temperature-rise distributions, $\alpha = 0°$.

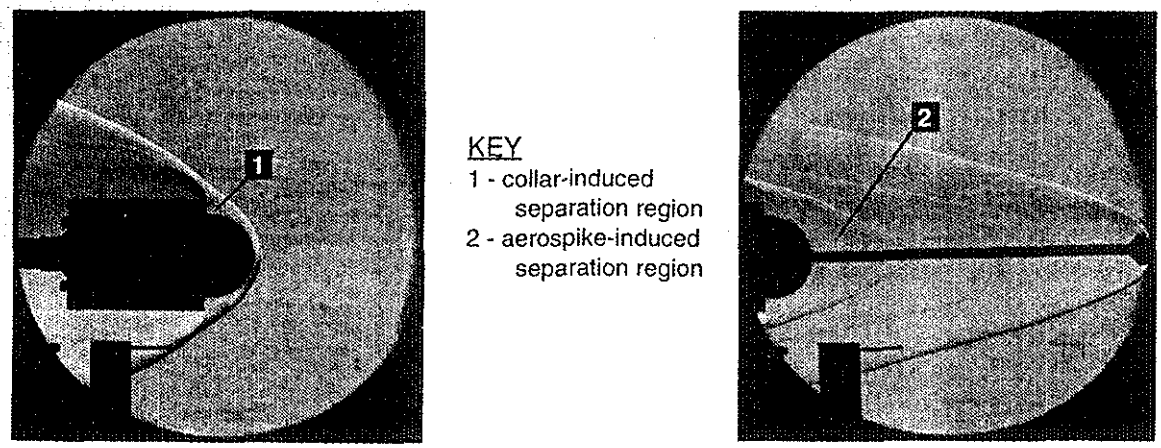

Figure 6c. Comparison of spike-off vs. spike-on schlieren flowfield photographs, $\alpha = 0°$.

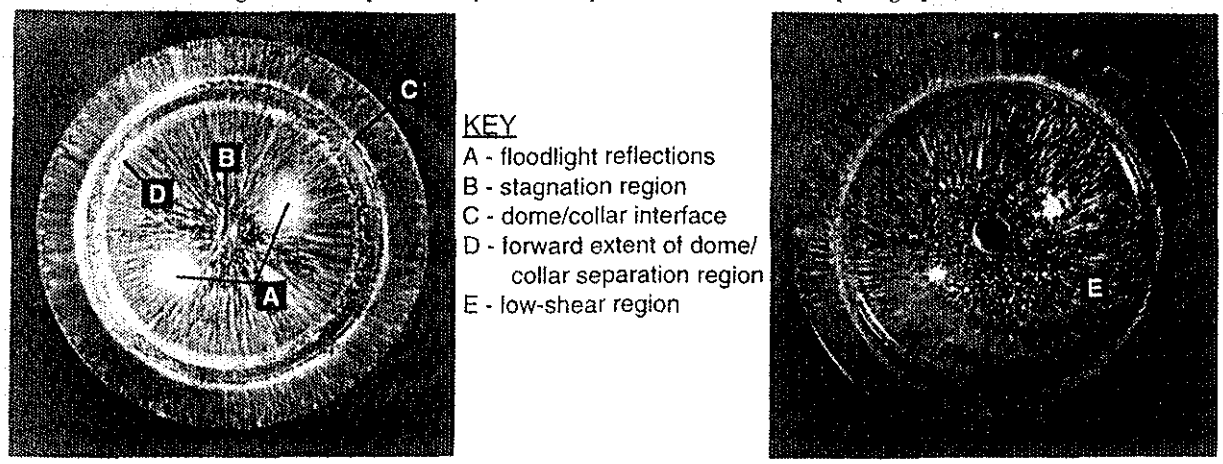

Figure 6d. Comparison of spike-off vs. spike-on surface oil-flow photographs, $\alpha = 0°$.

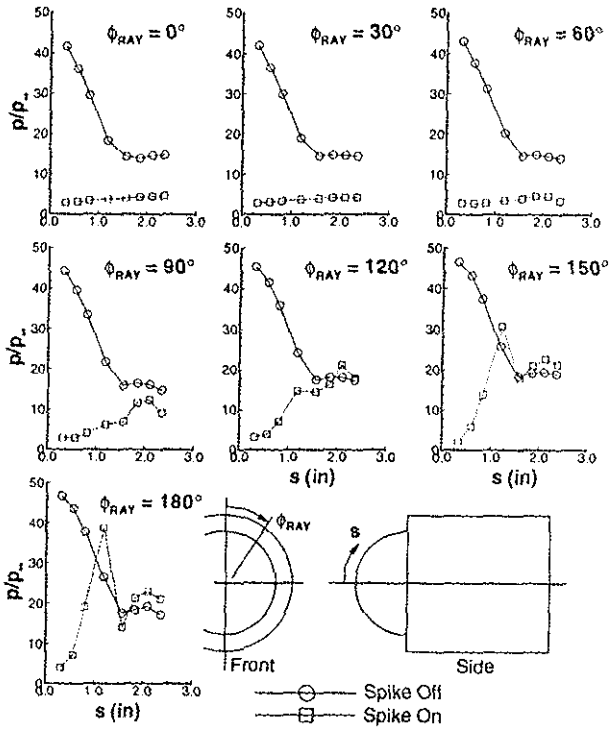

Figure 7a. Comparison of spike-off vs. spike-on surface pressure distributions, $\alpha = 5°$.

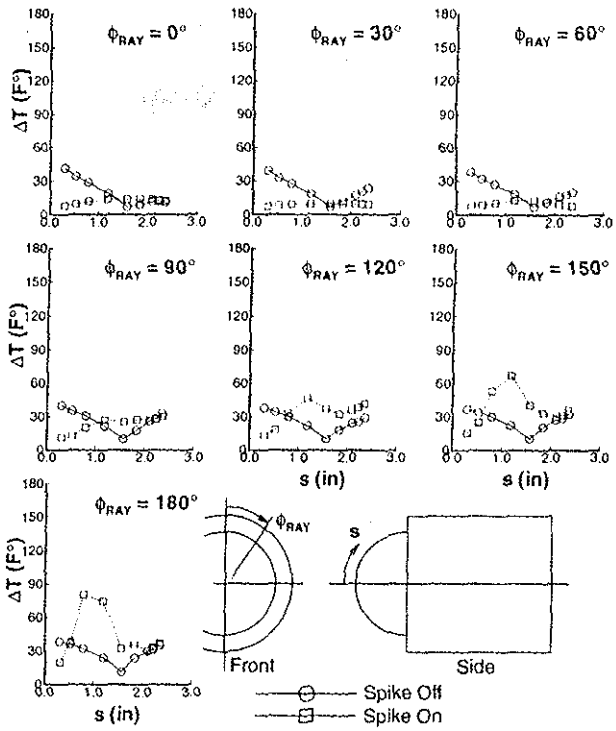

Figure 7b. Comparison of spike-off vs. spike-on surface temperature-rise distributions, $\alpha = 5°$.

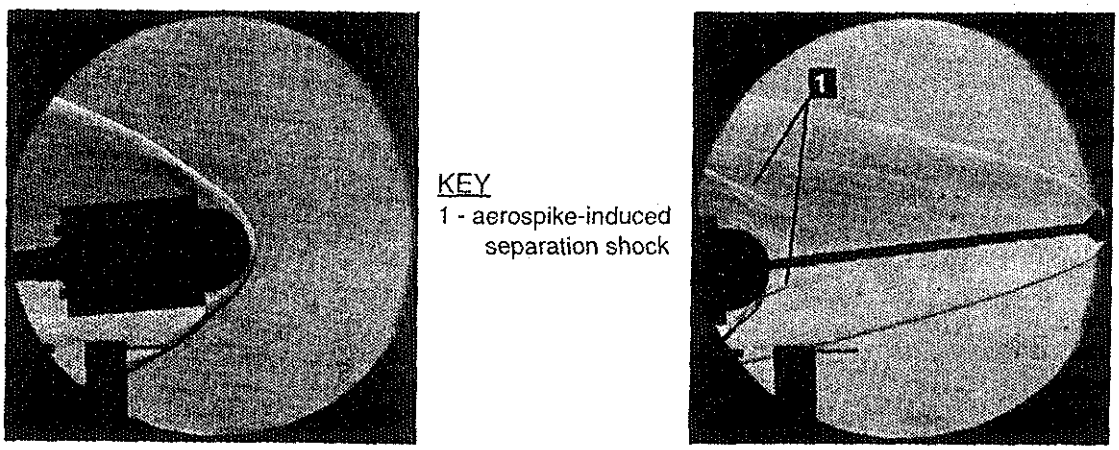

Figure 7c. Comparison of spike-off vs. spike-on schlieren flowfield photographs, $\alpha = 5°$.

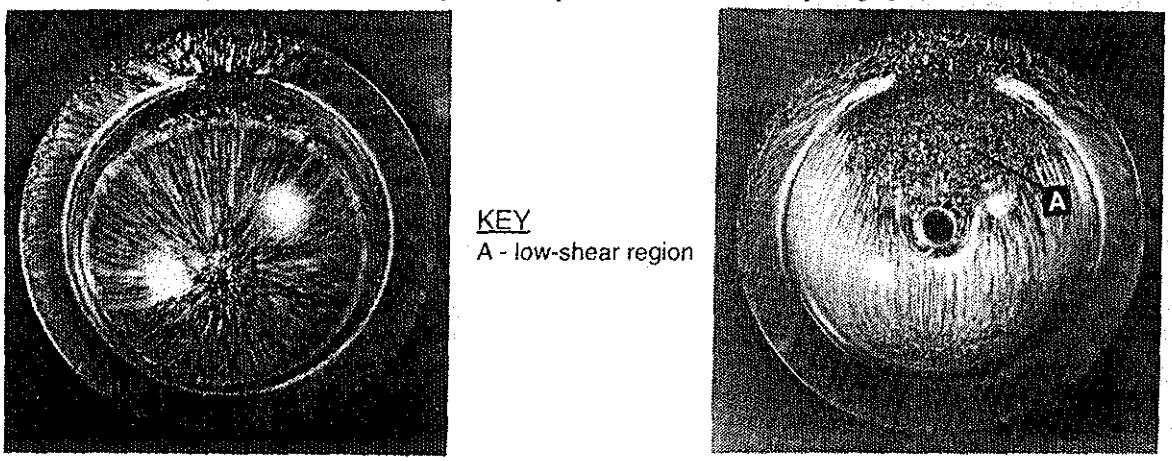

Figure 7d. Comparison of spike-off vs. spike-on surface oil-flow photographs, $\alpha = 5°$.

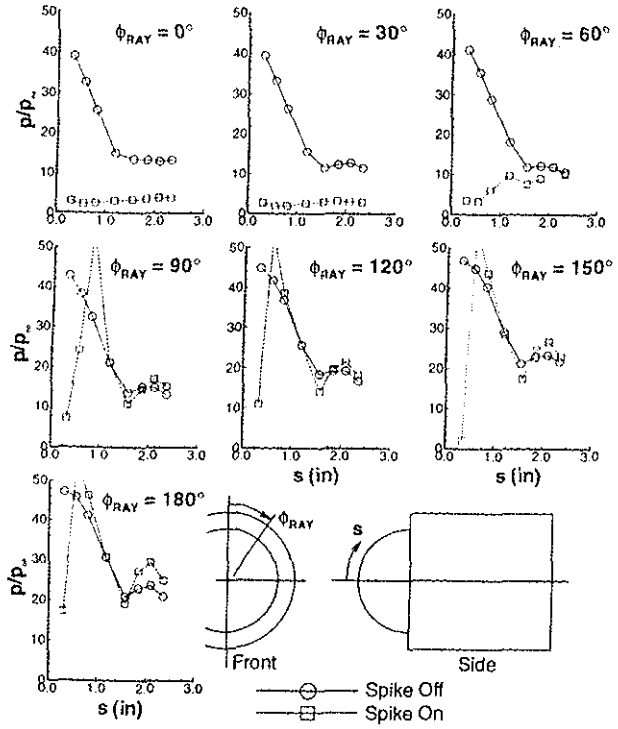

Figure 8a. Comparison of spike-off vs. spike-on surface pressure distributions, $\alpha = 10°$.

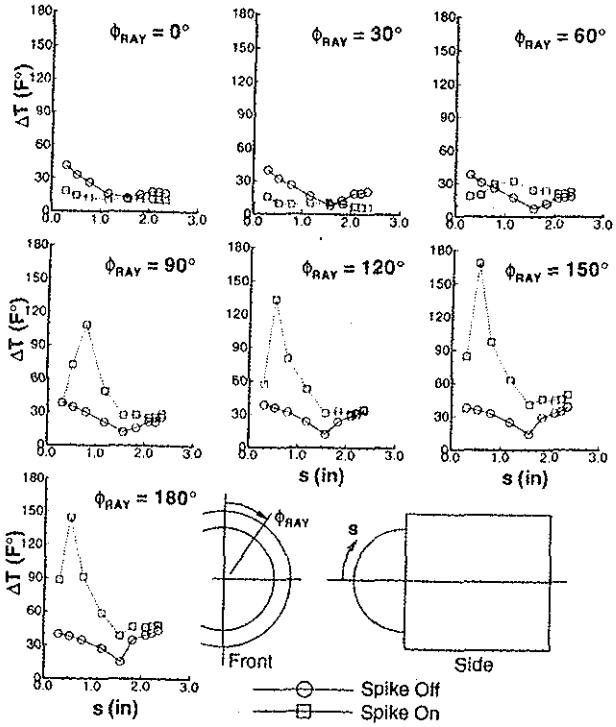

Figure 8b. Comparison of spike-off vs. spike-on surface temperature-rise distributions, $\alpha = 10°$.

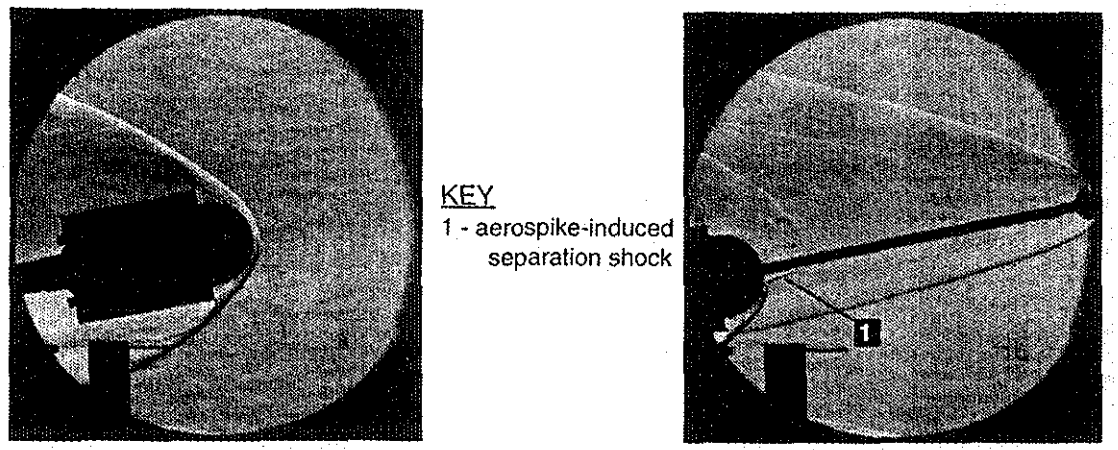

Figure 8c. Comparison of spike-off vs. spike-on schlieren flowfield photographs, $\alpha = 10°$.

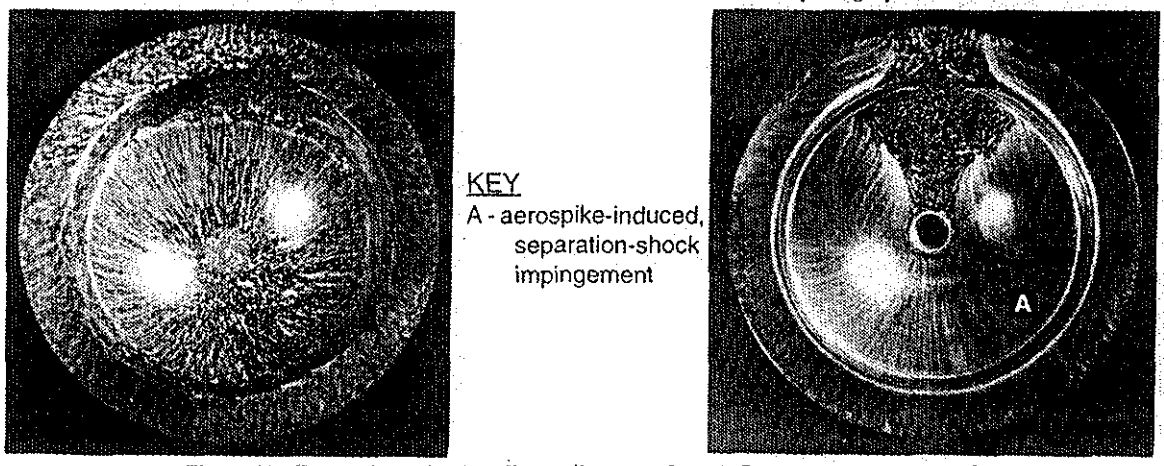

Figure 8d. Comparison of spike-off vs. spike-on surface oil-flow photographs, $\alpha = 10°$.

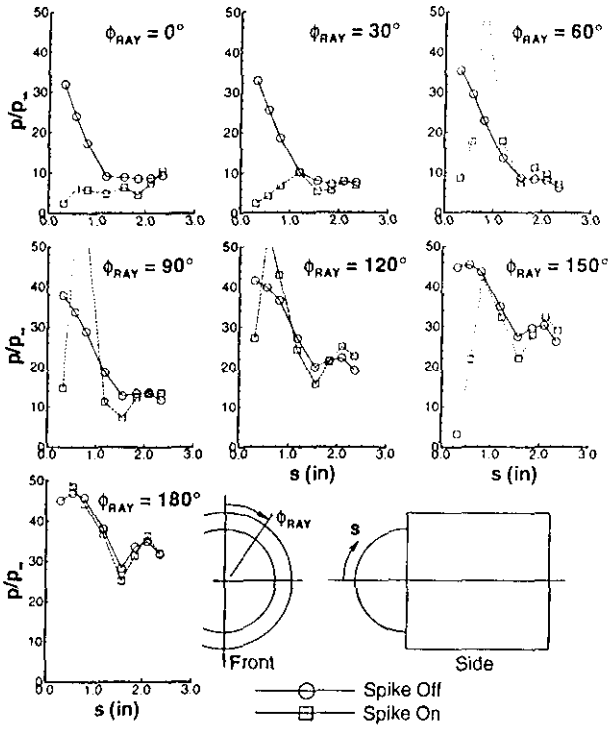

Figure 9a. Comparison of spike-off vs. spike-on surface pressure distributions, $\alpha = 20°$.

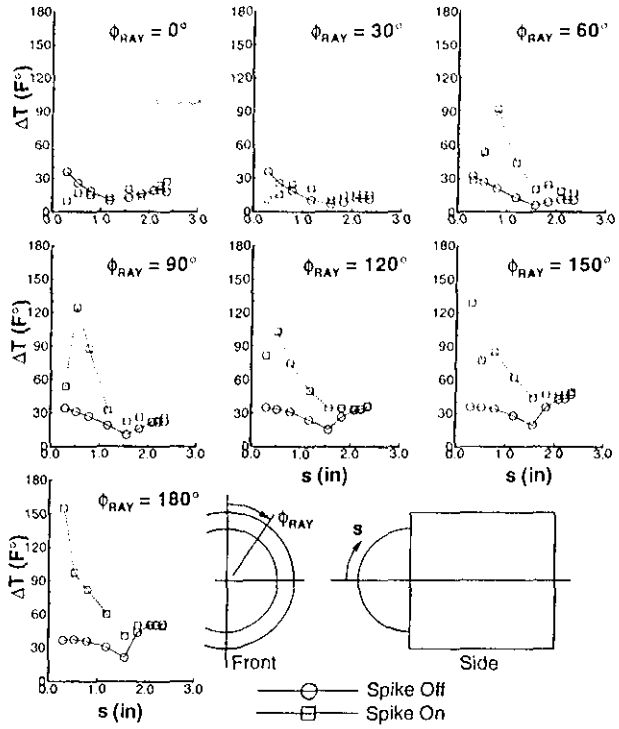

Figure 9b. Comparison of spike-off vs. spike-on surface temperature-rise distributions, $\alpha = 20°$.

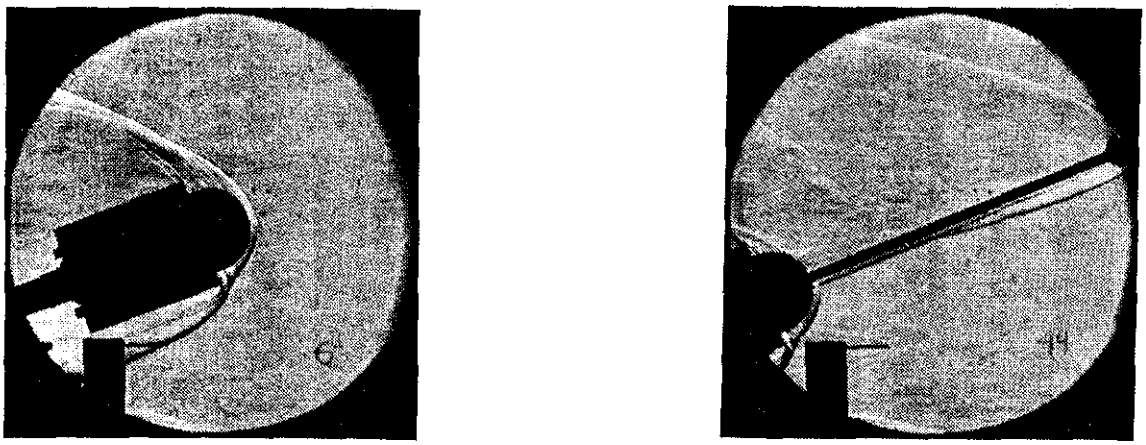

Figure 9c. Comparison of spike-off vs. spike-on schlieren flowfield photographs, $\alpha = 20°$.

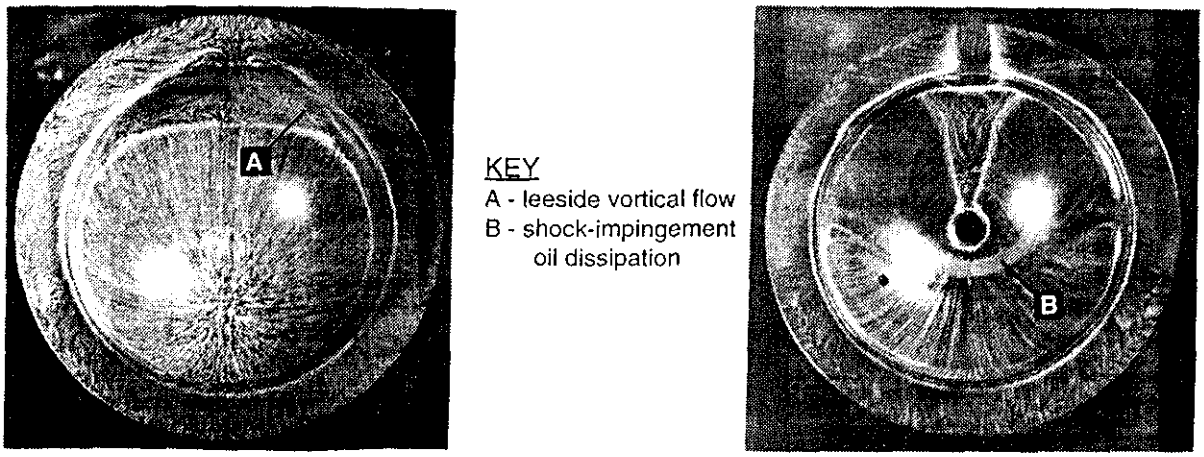

Figure 9d. Comparison of spike-off vs. spike-on surface oil-flow photographs, $\alpha = 20°$.

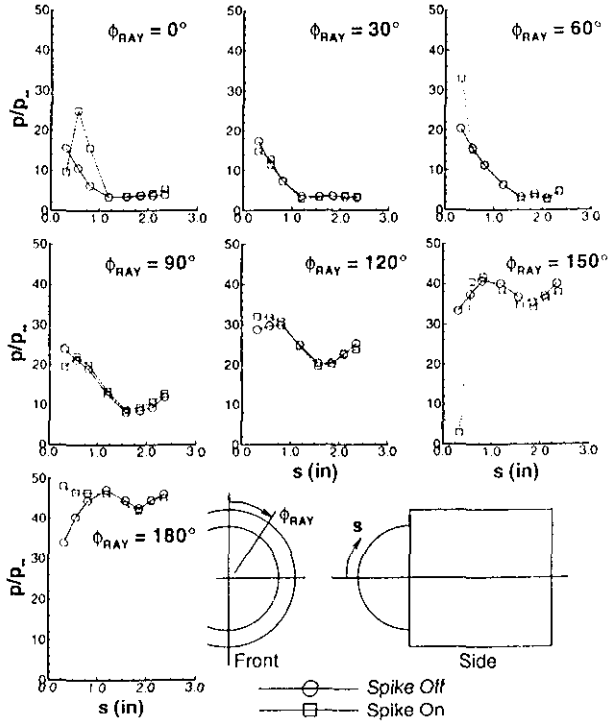

Figure 10a. Comparison of spike-off vs. spike-on surface pressure distributions, $\alpha = 40°$.

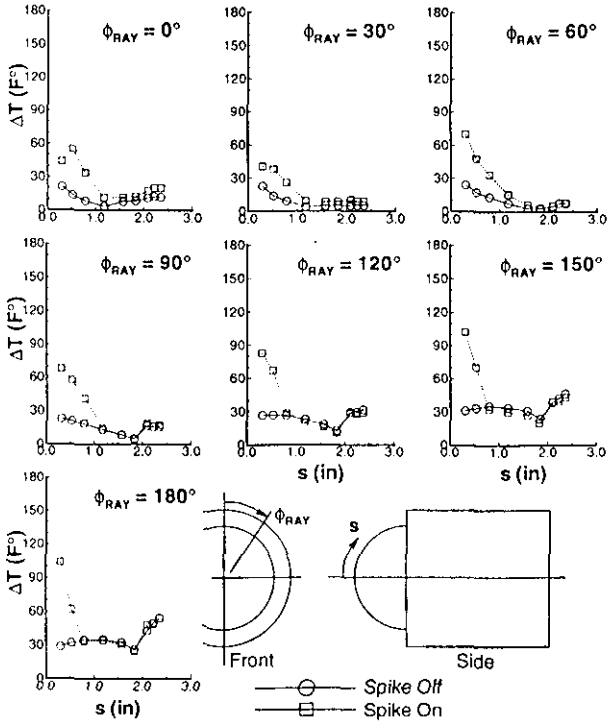

Figure 10b. Comparison of spike-off vs. spike-on surface temperature-rise distributions, $\alpha = 40°$.

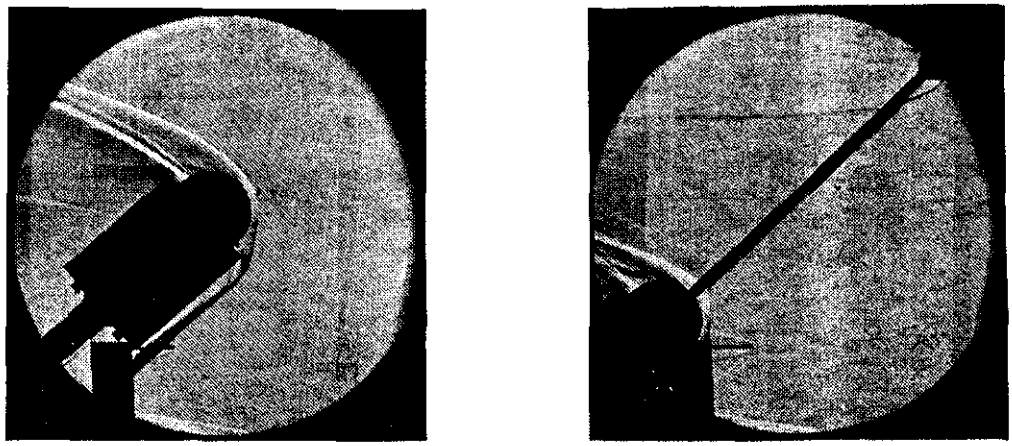

Figure 10c. Comparison of spike-off vs. spike-on schlieren flowfield photographs, $\alpha = 40°$.

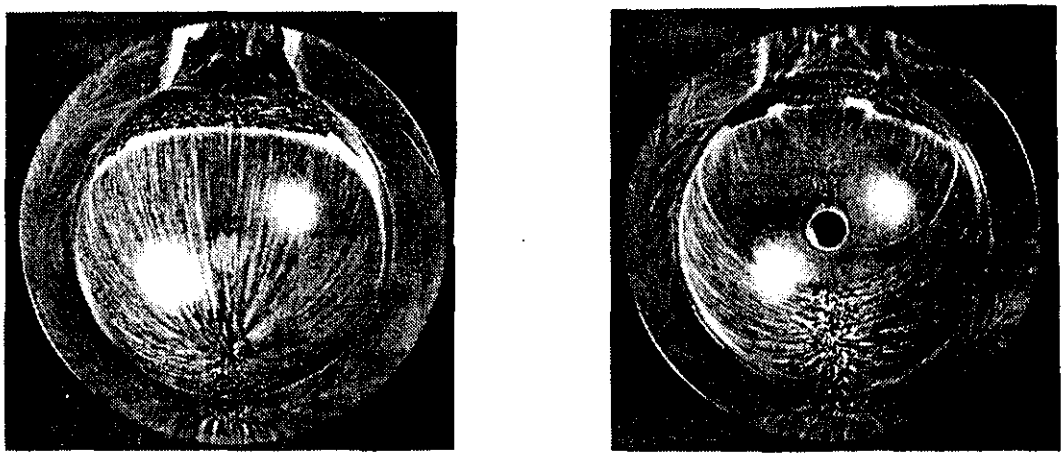

Figure 10d. Comparison of spike-off vs. spike-on surface oil-flow photographs, $\alpha = 40°$.